NONPRINCIPAL PLANE SCATTERING OF FLAT PLATES AND PATTERN CONTROL OF HORN ANTENNAS

Semiannual Report

PART A

Constantine A. Balanis and Lesley A. Polka

August 1, 1988 - January 31, 1989

PART B

Constantine A. Balanis and Kefeng Liu

August 1, 1988 - January 31, 1989

Department of Electrical and Computer Engineering
Arizona State University
Tempe, AZ 85287

Grant No. NAG-1-562
National Aeronautic and Space Administration
Langley Research Center
Hampton, VA 23665

ABSTRACT

Using the geometrical theory of diffraction, the traditional method of high frequency scattering analysis, the prediction of the radar cross section of a perfectly conducting, flat, rectangular plate is limited to principal planes. Part A of this report predicts the radar cross section in nonprincipal planes using the method of equivalent currents. This technique is based upon an asymptotic end-point reduction of the surface radiation integrals for an infinite wedge and enables nonprincipal plane prediction. The predicted radar cross sections for both horizontal and vertical polarizations are compared to moment method results and experimental data from Arizona State University's anechoic chamber.

In part B of this report, a variational calculus approach to the pattern control of the horn antenna is outlined. The approach starts with the optimization of the aperture field distribution so that the control of the radiation pattern in a range of directions can be realized. A control functional is thus formulated. Next, a spectral analysis method is introduced to solve for the eigenfunctions from the extremal condition of the formulated functional. Solutions to the optimized aperture field distribution are then obtained.

Part A

Nonprincipal Plane Scattering of Flat Plates

I. Introduction

The design of low-observable vehicles, with a reduced radar cross section (RCS), is a problem of current interest within the scientific and military communities. The parameters of interest in RCS reduction are the material composition and shape of the target. The importance of each of these factors varies with the type of radar used for detection. Over-the-horizon radar, used for long-range surveillance, operates at low frequencies in the VHF region or lower, resulting in targets on the order of one or two wavelengths in size. The material composition of the target is the chief factor in RCS minimization in this frequency range. Other radars, such as airborne systems, operate at higher frequencies, usually above 1 GHz, rendering targets several wavelengths in size. In this frequency range the shape of the target takes precedence over material composition in RCS determination.

For high-frequency scattering prediction, each part of the body of interest can be viewed as an independent scatterer. RCS prediction at high frequencies thus involves decomposing the target into simple geometric entities, calculating the RCS of each entity, and then appropriately summing the individual predictions

to achieve an overall RCS. The accurate modeling of simple shapes is, therefore, critical. One geometry of particular interest is the perfectly conducting, flat, rectangular plate.

The Geometrical Theory of Diffraction (GTD) [1] and the Uniform Theory of Diffraction (UTD) [2], the traditional high-frequency modeling techniques, accurately predict the scattering from the flat plate in the principal plane away from grazing and near-grazing incidences [3]. The GTD/UTD results are inaccurate in directions away from the Keller cone of diffracted rays; therefore, this method cannot be used in modeling the scattering patterns in nonprincipal planes, or planes not parallel to one of the edges of the plate. Ross's analysis [3] of the principal plane scattering of the plate involves truncating the two-dimensional GTD solution for an infinite, perfectly conducting, finite-width strip. This truncation does not account for the presence of the two edges parallel to the plane of incidence and diffraction. These edges are not critical in scattering near normal incidence; but as the grazing and near-grazing directions are approached, the role of these two edges in the scattering mechanism becomes more important. Because the GTD solution does not include these edges, the predictions near grazing and at grazing do not agree with experimental results.

Sikta [4] developed another high-frequency analysis using the method of equivalent currents. By dividing the plate into strips

that approach zero thickness as a limit and summing the contributions from each strip, the RCS for principal and nonprincipal scattering planes can be calculated by varying the orientation of the strips. The RCS of each strip is calculated using the method of equivalent currents.

The method of equivalent currents lacks the simplicity of the GTD approach to scattering prediction and the insight into physical scattering points that GTD provides. Despite these drawbacks, it has two distinct advantages over GTD. First, it can be used to correct for axial caustics encountered by GTD [5]. Second, and more importantly for the modeling of the flat rectangular plate, the method of equivalent currents can be used to predict scatttering in directions away from the Keller cone.

The general theory behind the method of equivalent currents is that the fields scattered by an object are approximated by the fields radiated by nonphysical electric and magnetic currents placed along the edges of the scatterer. The crucial problem in scattering prediction using the method of equivalent currents is, therefore, the formulation of accurate equivalent currents. Several different versions of equivalent currents exist. One of the first references to the method of equivalent currents is in Millar's work on scattering by a circular aperture in a perfectly conducting, plane, infinite screen with plane wave incidence [6]. These equivalent currents are derived by extracting the first term in the asymptotic expansion of the exact Sommerfeld half-plane

solution. The extent of the applications of Millar's equivalent currents is limited.

Ryan and Peters formulated equivalent currents using the GTD diffraction coefficient [5]. Conceptually these are the same as Millar's currents, although they differ in form. These successfully correct for axial caustics [5] and predict radiation patterns of rectangular waveguides [7] and horn antennas [8]. Because of the nature of the GTD diffraction coefficient, their equivalent currents are limited to scattering prediction on the Keller cone. Despite this limitation, Sikta predicts nonprincipal plane scattering from flat plates using these equivalent currents by careful orientation of the strips that divide the plate.

Michaeli formulated more rigorous equivalent currents that are valid for scattering directions away from the Keller cone of diffracted rays [9-11]. These currents are derived using an asymptotic end-point reduction of the surface radiation integral to a line radiation integral. The GTD equivalent currents [9] contain infinite discontinuities at certain directions of incidence and observation. By considering the integration across the surface at a skew angle, the Physical Optics/Physical Theory of Diffraction (PO/PTD) equivalent currents [10-11] remove all singularities, except the Ufimtsev singularity for forward scattering at grazing incidence.

This work examines the monostatic RCS of the perfectly conducting, flat, rectangular plate using the GTD [9] and PO/PTD

[10-11] equivalent currents of Michaeli. Both horizontal and vertical polarizations are considered. Scattering in nonprincipal planes is emphasized. Results are compared with data from moment method (MM) computations and experimental measurements performed in Arizona State University's (ASU's) compact range.

II. Theory

A. RCS Calculation

The plate geometry, shown in Fig. 1, is oriented so that the x-z and y-z planes correspond to principal planes. Nonprincipal planes are designated by a tilt angle ϕ', measured from the positive x axis. RCS values in a designated plane are calculated as a function of θ', measured from the positive z axis. An $e^{j\omega t}$ time convention is assumed and suppressed throughout.

The standard definition of the three-dimensional RCS is [12]:

$$\sigma_{3\text{-}D} = \lim_{r\to\infty} \left\{ 4\pi r^2 \frac{|\underline{E}_s|^2}{|\underline{E}_i|^2} \right\} \tag{1}$$

This definition implies that the observation point is in the far-field region, or a distance of at least $2D^2/\lambda$ from the target where D is the largest dimension of the target.

Both horizontal and vertical polarizations are considered. For the horizontal polarization the incident electric and magnetic fields are:

$$\underline{E}_i = \hat{a}_\phi \, E_o e^{-jk\circ r} \tag{2a}$$

$$\underline{H}_i = \hat{a}_\theta \, E_o (1/\eta) e^{-jk\circ r} \tag{2b}$$

The fields for vertical polarization are:

$$\underline{E}_i = \hat{a}_\theta \, E_o e^{-jk\circ r} \tag{2c}$$

$$\underline{H}_i = -\hat{a}_\phi E_o (1/\eta) e^{-jk\circ r} \tag{2d}$$

$\hat{a}_\phi$ and $\hat{a}_\theta$ are the standard directional unit vectors in the spherical coordinate system, and $\underline{k}$ is the wavenumber, $2\pi/\lambda$, in the direction of propagation.

In order to simplify the analysis for the rectangular plate, the incident fields will be transformed to the rectangular coordinate system. The position vector $\underline{r}$ is:

$$\underline{r} = \hat{a}_x x + \hat{a}_y y + \hat{a}_z z \tag{3}$$

The propagation vector $\underline{k}$ for the incident field is:

$$\underline{k} = -k\hat{a}_r = -k(\hat{a}_x \sin\theta\cos\phi + \hat{a}_y \sin\theta\sin\phi + \hat{a}_z \cos\theta) \tag{4}$$

With respect to the rectangular coordinate system, the incident fields are:

Horizontal Polarization

$$\underline{E}_i = E_o e^{jk(x\sin\theta\cos\phi + y\sin\theta\sin\phi + z\cos\theta)} [-\hat{a}_x \sin\phi + \hat{a}_y \cos\phi\ ] \tag{5a}$$

$$\underline{H}_i = E_o (1/\eta) e^{jk(x\sin\theta\cos\phi + y\sin\theta\sin\phi + z\cos\theta)} \times [\hat{a}_x \cos\theta\cos\phi + \hat{a}_y \cos\theta\sin\phi + \hat{a}_z \sin\theta\ ] \tag{5b}$$

Vertical Polarization

$$\underline{E}_i = E_o e^{jk(x\sin\theta\cos\phi + y\sin\theta\sin\phi + z\cos\theta)} \times [\hat{a}_x \cos\theta\cos\phi + \hat{a}_y \cos\theta\sin\phi + \hat{a}_z \sin\theta\ ] \tag{5c}$$

$$\underline{H}_i = -E_o (1/\eta) e^{jk(x\sin\theta\cos\phi + y\sin\theta\sin\phi + z\cos\theta)} \times [-\hat{a}_x \sin\phi + \hat{a}_y \cos\phi\ ] \tag{5d}$$

To calculate the scattered fields, a vector potential approach is used. The electric field components in the far zone are approximated by [13]:

$$E_r \cong 0 \tag{6a}$$

$$E_\theta \cong -j\omega\ [A_\theta + \eta F_\phi] \tag{6b}$$

$$E_\phi \cong -j\omega\ [A_\phi - \eta F_\theta] \tag{6c}$$

The magnetic ($\underline{A}$) and the electric ($\underline{F}$) vector potentials are defined as [13]:

$$\underline{A} = \frac{\mu}{4\pi} \int_C \underline{I}(x',y',z')\ \frac{e^{-jkR}}{R}\ dl' \tag{7a}$$

$$\underline{F} = \frac{\epsilon}{4\pi} \int_C \underline{M}(x',y',z')\ \frac{e^{-jkR}}{R}\ dl' \tag{7b}$$

$\underline{I}$ and $\underline{M}$ are the equivalent electric and magnetic currents, respectively, which are placed along the perimeter of the scatterer. They radiate into free space according to (6) and (7) and approximate the scattered fields. The geometry for far-field scattering is shown in Fig. 2. The location of the scatterer is designated by primed coordinates and the observation location by unprimed coordinates. Integration is along C, the edge of the scatterer. The distance from the source point to the observation point is R, represented by

$$R=|\underline{R}|=|\underline{r}-\underline{r}'| \tag{8}$$

The location vectors of the source and observation points with respect to the origin of the coordinate system are $\underline{r}'$ and $\underline{r}$, respectively.

For far-field scattering the following simplifications can be made:

$$R \cong r - r'\cos\vartheta = r - \underline{r}' \circ \hat{a}_r \quad \text{(for phase variations)} \tag{9a}$$

$$R \cong r \quad \text{(for amplitude variations)} \tag{9b}$$

For the flat plate centered at the origin of the rectangular coordinate system:

$$\underline{r}' = \hat{a}_x x + \hat{a}_y y \tag{10}$$

Thus, for phase variations:

$$R \cong r - x\sin\theta\cos\phi - y\sin\theta\sin\phi \tag{11}$$

By substituting (9b) and (11) into (7a) and (7b), the vector potentials for the flat plate become:

$$\underline{A} = \frac{\mu}{4\pi}\frac{e^{-jkr}}{r}\int_c \underline{I}(x,y,z)e^{jk(x\sin\theta\cos\phi + y\sin\theta\sin\phi)}dl \tag{12a}$$

$$\underline{F} = \frac{\varepsilon}{4\pi}\frac{e^{-jkr}}{r}\int_c \underline{M}(x,y,z)e^{jk(x\sin\theta\cos\phi + y\sin\theta\sin\phi)}dl \tag{12b}$$

These integrals are evaluated along the perimeter of the plate. To simplify the derivation, each integral is represented as a sum of four integrals, each corresponding to an edge of the plate. For the plate the integration is of simple form, and the potentials can be expressed in closed form. $\underline{I}$ and $\underline{M}$ must be determined separately for each edge taking into account the individual geometries. Each edge is viewed as the truncation of an infinite wedge, which reduces to a half plane for the flat plate. The formulation for a general half plane follows.

B. Equivalent Currents

1. Geometry

The general wedge configuration used for both the GTD [9] and PO/PTD [10-11] equivalent currents is shown in Fig. 3. For a half plane, n, which denotes the wedge angle, is 2. There are several directional vectors and angles which are crucial to the

development. The directional vectors are:

$\hat{s}'$= unit vector in the direction of incidence

$\hat{s}$= unit vector in the direction of observation

$\hat{t}$= unit vector tangent to the edge of interest, directed so that it encircles the scatterer in a counterclockwise manner

$\hat{n}$= unit vector normal to the edge of interest, lying on the upper face

The angles are:

β'= angle between $\hat{s}'$ and the edge

β = angle between $\hat{s}$ and the edge

ϑ'= angle between the upper face and the edge-fixed plane of incidence

ϑ = angle between the upper face and the edge-fixed plane of observation

α = skew angle for integration across the surface

In terms of the directional vectors, the angles are:

$$\beta' = \cos^{-1}(\hat{s}' \circ \hat{t}) \tag{13a}$$

$$\beta = \cos^{-1}(\hat{s} \circ \hat{t}) \tag{13b}$$

$$\vartheta' = \cos^{-1}\left\{\left[\frac{\hat{s}' \times \hat{t}}{|\hat{s}' \times \hat{t}|} \times \hat{t}\right] \circ \hat{n}\right\} \tag{13c}$$

$$\vartheta = \cos^{-1}\left\{\left[\frac{\hat{s} \times \hat{t}}{|\hat{s} \times \hat{t}|} \times \hat{t}\right] \circ \hat{n}\right\} \tag{13d}$$

This report considers only backscattering from the flat, rectangular plate. For backscattering, $\vartheta=\vartheta'$, $\beta=\pi-\beta'$, and $\hat{s}=-\hat{s}'$. For the flat plate this vector is:

$$\hat{s}' = -\hat{a}_r = -\hat{a}_x \sin\theta\cos\phi - \hat{a}_y \sin\theta\sin\phi - \hat{a}_z \cos\theta \tag{14}$$

A different set of angles must be formulated for each edge. The vectors for each edge are:

Edge 1: $\hat{t}_1 = \hat{a}_y$ $\hat{n}_1 = -\hat{a}_x$

Edge 2: $\hat{t}_2 = -\hat{a}_y$ $\hat{n}_2 = \hat{a}_x$

Edge 3: $\hat{t}_3 = -\hat{a}_x$ $\hat{n}_3 = -\hat{a}_y$

Edge 4: $\hat{t}_4 = \hat{a}_x$ $\hat{n}_4 = \hat{a}_y$

For each edge the tangential components of the incident electric and magnetic fields are needed to determine the corresponding equivalent currents. The tangential electric field component at the edge of interest is:

$$E_i^{tan} = \underline{E}_i \circ \hat{t} \tag{15a}$$

and the magnetic field component is:

$$H_i^{tan} = \underline{H}_i \circ \hat{t} \tag{15b}$$

The individual current components are easily determined by substitution of the incident field components and directional angles into the appropriate current equation.

2. GTD Equivalent Currents

The GTD equivalent currents [9] are based upon an asymptotic endpoint evaluation of the surface radiation integrals for a wedge. The integration across the surface is along a coordinate normal to the edge of the wedge. This choice of integration coordinate results in infinite discontinuities in the calculated fields when bistatic calculations are made. The monostatic results using these currents, however, avoid infinities.

The expressions for the equivalent electric (I) and magnetic

(M) currents for a general wedge configuration are quite long and are, therefore, not repeated here. For backscattering ($\vartheta=\vartheta'$, $\beta=\pi-\beta$, and $\hat{s}=-\hat{s}'$) from a half plane (n=2), they simplify considerably, and they take the forms of:

Electric Equivalent Current:

$$I=\frac{1}{jk\sin^2\beta'}\left\{E_i^{tan}\ \frac{(\cos\vartheta-1)}{\eta\cos\vartheta}-H_i^{tan}\ \frac{2\cos\beta'(1+\cos\vartheta)}{\sin\vartheta}\right\} \qquad (16a)$$

Magnetic Equivalent Current:

$$M=H_i^{tan}\ \frac{\eta(1+\cos\vartheta)}{jk\sin^2\beta'\cos\vartheta} \qquad (16b)$$

An interesting aspect of these currents is that the electric current depends on both the incident tangential electric and magnetic fields. Earlier versions formulated by Millar [6] and Ryan and Peters [5] do not contain this dependence, which makes them invalid in directions away from the Keller cone of diffracted rays. The currents of (16a) and (16b) are valid in all directions of observation.

3. PO/PTD Equivalent Currents

In order to correct for the discontinuities incurred by the GTD equivalent currents, Michaeli derived new currents [10-11] that incorporated integration across the wedge at a skew angle rather than in a direction normal to the edge under consideration. The skew coordinate of integration corresponds to the grazing diffracted ray, which is shown in Fig. 3. The angle of this ray

with respect to the edge is β', the same as the angle that the incident ray makes with the edge. This choice of geometry for the integration eliminates all singularities except the Ufimtsev forward scatter singularity due to grazing incidence.

The PO/PTD analysis consists of PO and PTD current components. The PO components [10] account for the radiation of the surface currents that would be present if the scatterer were infinite in extent. The PTD components [11] account for the finite boundaries of the scatterer. The sum of these components is finite in all directions except for the Ufimtsev singularity for forward scatter and grazing incidence.

A. PO Components

The forms of the general PO equivalent currents [10] are rather tedious expressions involving the modified Fresnel transition function. For far-field, plane-wave backscattering from a half plane, however, the Fresnel transition function can be replaced by its asymptotic expansion. In this case the components simplify to:

$$I^{po} = \frac{j}{k\eta} \frac{\sin\alpha\sin\vartheta'}{\sin\beta'} (\hat{t}\circ\underline{E}_i) \frac{1}{(\sin\theta\sin\beta'\cos\vartheta' - \cos\theta\cos\beta')} \qquad (17a)$$

$$M^{po} = -\frac{j\eta}{k} \frac{\sin\alpha\sin\vartheta'}{\sin\beta'} (\hat{t}\circ\underline{H}_i) \frac{1}{(\sin\theta\sin\beta'\cos\vartheta' - \cos\theta\cos\beta')} \qquad (17b)$$

The angle α denotes the direction of the transverse coordinate for integration. For the analysis in this work, α was taken to be 90°, corresponding to integration normal to the plate

edge. Accurate results are obtained for α between ϕ and 90°.

B. PTD Components

The PTD components that must be added to the PO currents reduce to the following for backscattering from a half plane:

$$I^{ptd} = \frac{j\sqrt{2}}{k\sin\beta'}\left\{ E_i^{tan} \frac{\sin(\vartheta'/2)}{\eta\sin\beta'(\cos\vartheta'-\cot^2\beta')} \times \left[\sqrt{1-\cos\vartheta'+2\cot^2\beta'} - \sqrt{2}\cos(\vartheta'/2)\right] + H_i^{tan} \frac{2\cos(\vartheta'/2)\cot\beta'}{\sqrt{1-\cos\vartheta'+2\cot^2\beta'}}\right\} \quad (18a)$$

$$M^{ptd} = H_i^{tan} \frac{j\eta\sin\vartheta'}{k\sin^2\beta'(\cos\vartheta'-\cot^2\beta')} \times \left\{1- \frac{\sqrt{2}\cos(\vartheta'/2)}{\sqrt{1-\cos\vartheta'+2\cot^2\beta'}}\right\} \quad (18b)$$

Note that, similar to the GTD electric currents, the PTD electric currents depend on both the incident electric and magnetic fields.

C. Assembly of Scattered Fields

The calculation of the RCS involves the assembling of the appropriate equations. First, calculate the currents for each edge of the plate using either the GTD currents of (16a) and (16b) or the PO/PTD currents of (17a)-(18b). To determine the tangential fields, use (15a) and (15b) and either (5a) and (5b) for horizontal polarization or (5c) and (5d) for vertical

polarization. Substitute the appropriate currents into (12a) and (12b) to obtain the vector potentials. Finally, substitute into (6b) and (6c) to obtain the electric field components.

Unlike the fields predicted by traditional GTD analysis, the scattered electric fields for both polarizations (as predicted by the proposed methods) include cross polarization terms. However, in the calculation of the RCS, only the primary polarization terms are considered. In other words, the E_ϕ components are used for horizontal polarization, and the E_θ components are used for vertical polarization.

A final note of interest in the RCS calculations using the equivalent currents method is that the fields must be multiplied by a factor 1/2 to obtain the correct magnitudes. This is a problem that Ryan and Peters [5] and Sikta [4] also encounter. Ryan and Peters were off by a factor of 1/2 elsewhere in their derivation and, therefore, did not recognize that the fields were double the correct values. Sikta pointed out their error and avoided the same problem by considering currents only along edges normal to the plane of incidence and diffraction in calculating the fields. One intuitive explanation for the necessity of the factor of 1/2 is that in placing currents along all four edges of the plate, the integration across the plate is performed twice, thus doubling the fields. For a four-sided parallelogram the compensating factor of 1/2 is easily justified. It is not clear what the correction factor should be in applying the equivalent

currents method to scatterers with more edges. This will be examined in our next period.

III. Results

Computations were made for a square plate with each side equal to 5.73 λ. The results of both the GTD and PO/PTD equivalent currents analyses were compared with MM computations and measurements performed at ASU's anechoic chamber. The results for scattering in a plane designated by $\phi'=30^{\circ}$ are shown in Fig. 4 for horizontal polarization and in Fig. 5 for vertical polarization. Figs. 6 and 7 are for horizontal and vertical polarization, respectively, at a tilt angle of $\phi'=45^{\circ}$.

The GTD equivalent currents results agree very well with the PO/PTD results, which is expected for monostatic calculations. For bistatic computations, the GTD currents encounter infinities in many directions. The PO/PTD formulation avoids infinities and, therefore, should be used. Since the GTD current expressions are less complicated than the PO/PTD components and are just as accurate, they are sufficient for monostatic work.

The equivalent currents predictions agree quite well with MM and experimental results up to 45° from normal incidence. As grazing incidence is approached, the equivalent currents patterns deviate from the MM and experimental. These discrepancies can probably be resolved by including corner diffraction [4] and higher-order terms [14].

The method of equivalent currents assumes that each edge is an infinite wedge; therefore, it does not properly account for the

joining of two edges at a corner. The need for some method of including the presence of the corners is illustrated in the results for a tilt angle of $\phi' = 45^{\circ}$ (Figs. 6 and 7), which corresponds to a plane of diffraction through both corners. These results deviate from the MM and experimental data to a greater extent than for $\phi' = 30^{\circ}$. No rigorously formulated corner diffraction coefficients currently exist. Sikta uses semi-empirical corner diffraction coefficients [4] and obtains accurate results despite the nonuniqueness of the fields in certain directions [14]. If carefully applied so that problem areas are avoided, this corner diffraction coefficient may lead to improved pattern results.

For vertical polarization higher-order diffractions dominate near grazing. The need to include higher-order terms is evident in comparing the vertical polarization results (Figs. 5 and 7) to the horizontal polarization results (Figs. 4 and 6). The results near grazing are much more accurate for horizontal than for vertical polarization. Michaeli formulates equivalent currents for second-order diffractions [14] that should improve the results near grazing incidence.

IV. Conclusions

The scattering patterns that can be accurately calculated using GTD, the traditional high-frequency prediction technique, are limited to principal planes. This work used the method of equivalent currents to extend scattering prediction to nonprincipal planes for monostatic RCS calculations. Results compared favorably with MM and experimental data away from grazing incidence. The addition of corner diffraction and higher-order terms was suggested to improve results near corners and grazing.

V. Publications

During this reporting period we had the following publications:

a. T. Griesser, C. A. Balanis, K. Liu, "RCS analysis and reduction for lossy dihedral corner reflectors," *Proc. IEEE*, May 1989 (special issue on RCS).

b. T. Griesser and C. A. Balanis, "Reflections, diffractions, and surface waves for an interior impedance wedge of arbitrary angle," accepted for publication in *IEEE Trans. Antennas Propagat.*

c. L. Polka and C. A. Balanis, "Nonprincipal plane scattering from perfectly conducting, flat, rectangular plates," submitted for presentation at the 1989 International IEEE Symposium on Antennas and Propagation.

VI. Future Work

The model for the perfectly conducting flat plate will be completed by adding corner diffraction and second-order terms. The equivalent currents model will be extended to bistatic scattering as well as to lossy plates. Finally, grazing incidence scattering will be examined more closely in an attempt to predict scattering at and near grazing as a function of tilt angle and plate size. Interesting trends have been experimentally observed for grazing incidence [3], but no rigorous theoretical models exist to match these results.

References

[1] J. B. Keller, "Geometrical theory of diffraction," *J. Opt. Soc. Amer.*, vol. 52, no. 2, pp. 116-130, Feb. 1962.

[2] R. G. Kouyoumjian and P. H. Pathak, "A uniform geometrical theory of diffraction for an edge in a perfectly conducting surface," *Proc. IEEE*, vol. 62, no. 11, pp. 1448-1461, Nov. 1964.

[3] R. A. Ross, "Radar cross section of rectangular flat plates as a function of aspect angle," *IEEE Trans. Antennas Propagat.*, vol. AP-14, no. 3, pp. 329-335, May 1966.

[4] F. A. Sikta, W. D. Burnside, T. Chu, and L. Peters, Jr., "First-order equivalent current and corner diffraction scattering from flat-plate structures," *IEEE Trans. Antennas Propagat.*, vol. AP-31, no. 4, pp. 584-589, July 1983.

[5] C. E. Ryan, Jr., and L. Peters, Jr., "Evaluation of edge-diffracted fields including equivalent currents for the caustic regions," *IEEE Trans. Antennas Propagat.*, vol. AP-17, no. 3, pp. 292-299, May 1969, (also corrections to this paper on p. 275, Mar. 1970)

[6] R. F. Millar, "An approximate theory of the diffraction of an electromagnetic wave by an aperture in a plane screen," *Proc. Inst. Elec. Eng.*, vol. 103, pt. C, pp. 177-185, Mar. 1956 (first published as Monograph 152R, Oct. 1955).

[7] C. E. Ryan, Jr., and R. C. Rudduck, "Radiation Patterns of Rectangular Waveguides," *IEEE Trans. Antennas Propagat.*, vol. AP-16, no. 4, pp. 488-489, July 1968.

[8] C. A. Mentzer, L. Peters, Jr., and R. C. Rudduck, "Slope diffraction and its application to horns," *IEEE Trans. Antennas Propagat.*, vol. AP-23, no. 2, pp. 153-159, Mar. 1975.

[9] A. Michaeli, "Equivalent edge currents for arbitrary aspects of observation," *IEEE Trans. Antennas Propagat.*, vol. AP-32, no. 3, pp. 252-258, Mar. 1984, (also corrections to this paper on p. 227, Feb. 1985)

[10] A. Michaeli, "Elimination of infinities in equivalent edge currents, part II: physical optics components," *IEEE Trans. Antennas Propagat.*, vol. AP-34, no. 8, pp. 1034-1037, Aug. 1986.

[11] A. Michaeli, "Elimination of infinities in equivalent edge currents, part I: fringe current components," *IEEE Trans. Antennas Propagat.*, vol. AP-34, no. 7, pp. 912-918, July 1986.

[12] G. T. Ruck, D. E. Barrick, and W. D. Stuart, "Ch. 2 - Theory," in *Radar Cross Section Handbook*, vol. 1, G. T. Ruck, Ed. New York: Plenum Press, 1970.

[13] C. A. Balanis, *Antenna Theory: Analysis and Design*. New York: John Wiley & Sons, Inc., 1982.

[14] A. Michaeli, "Equivalent currents for second-order diffraction by the edges of perfectly conducting polygonal surfaces," *IEEE Trans. Antennas Propagat.*, vol. AP-35, no. 2, pp. 183-190, Feb. 1987.

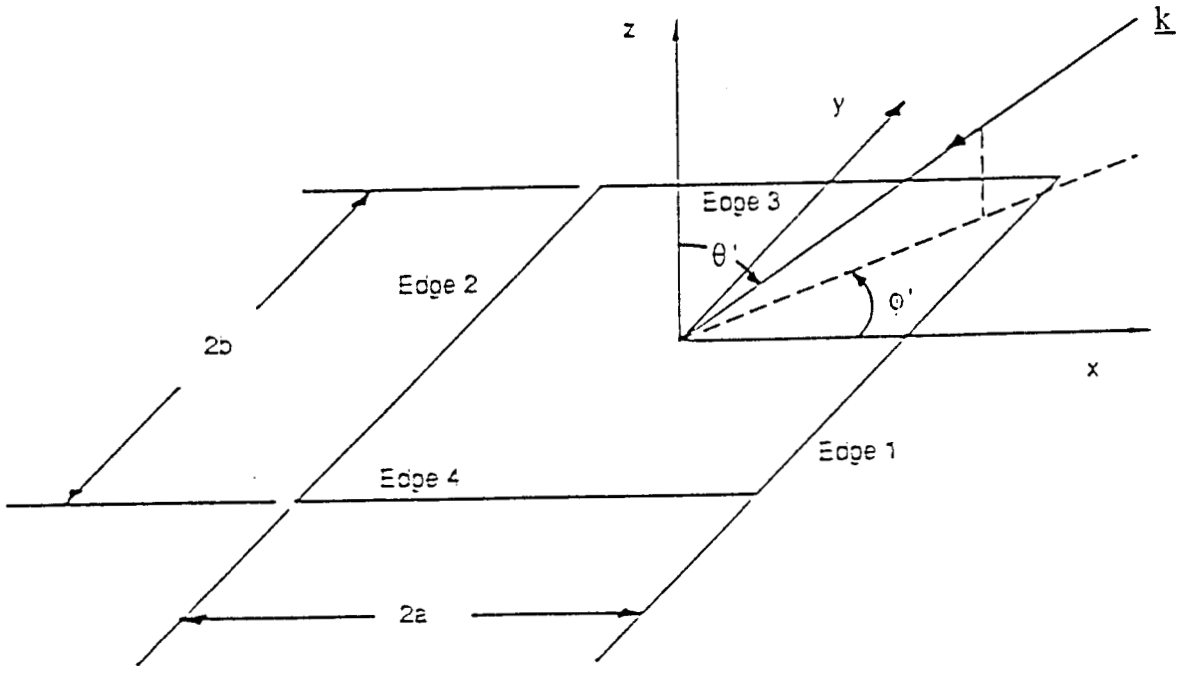

Fig. 1. Plate geometry for scattering.

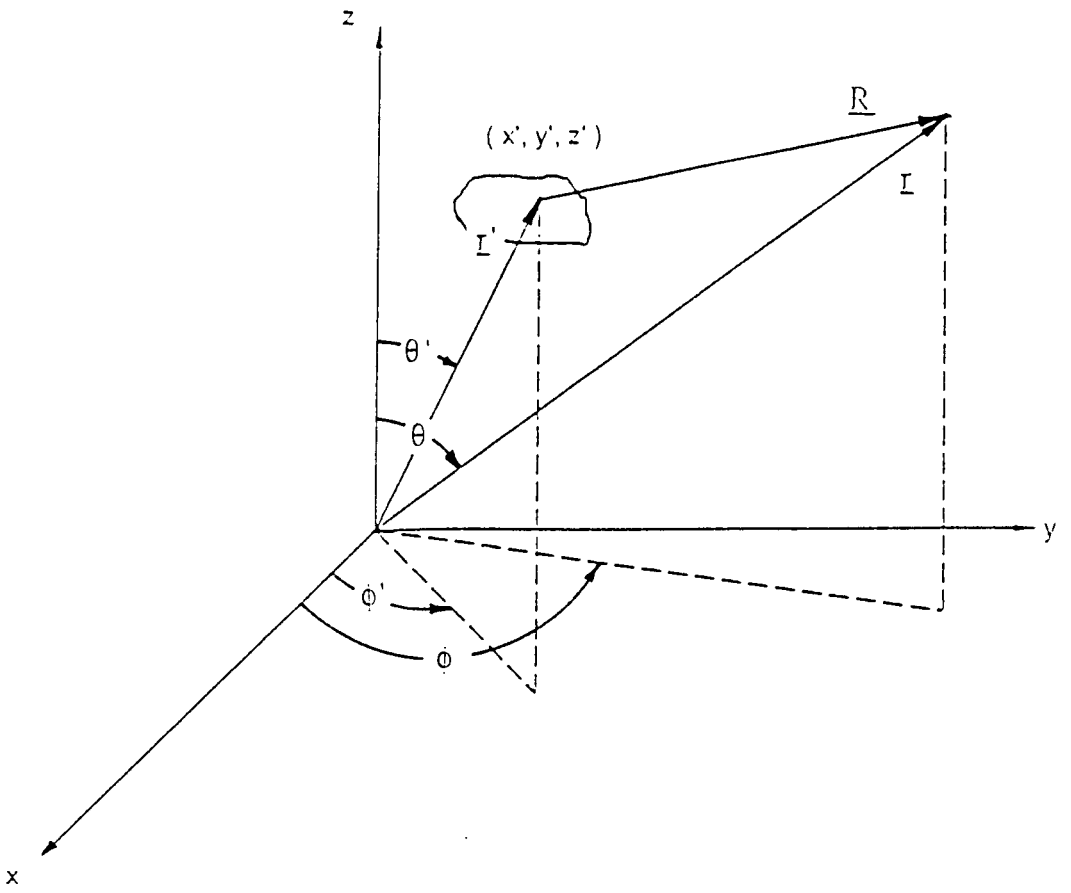

Fig. 2. Geometry for far-field radiation.

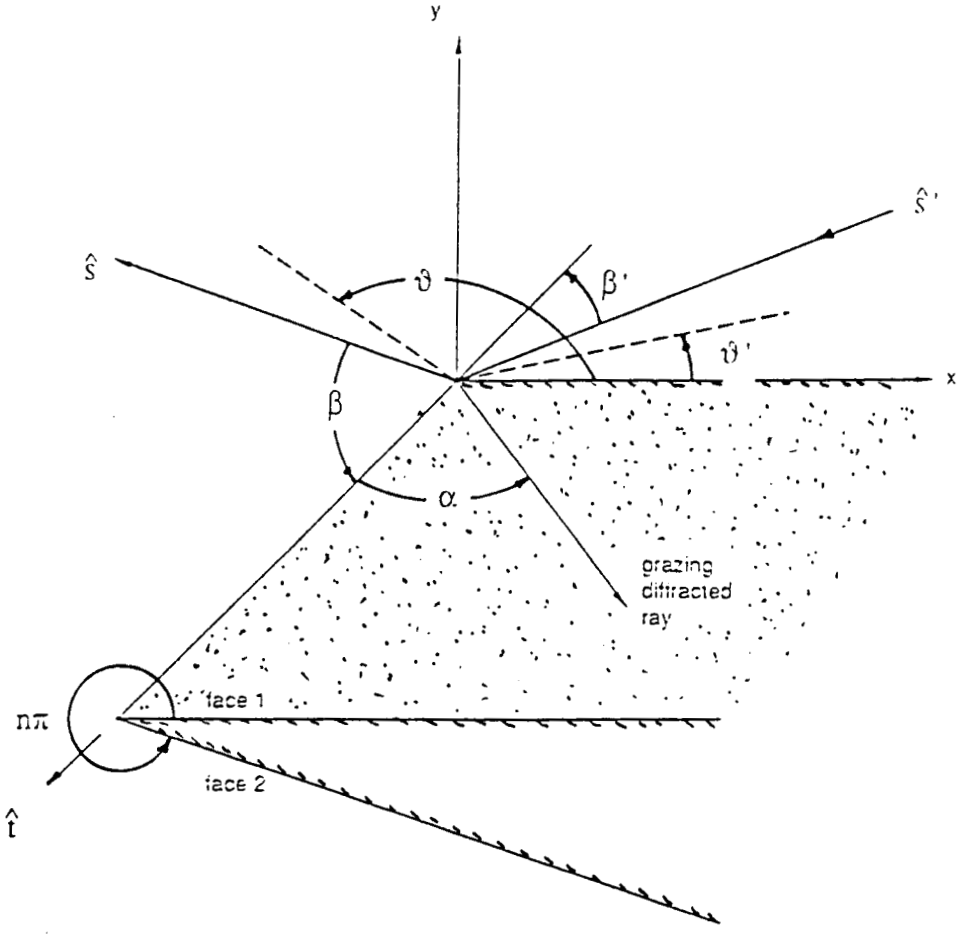

Fig. 3. General wedge geometry for scattering.

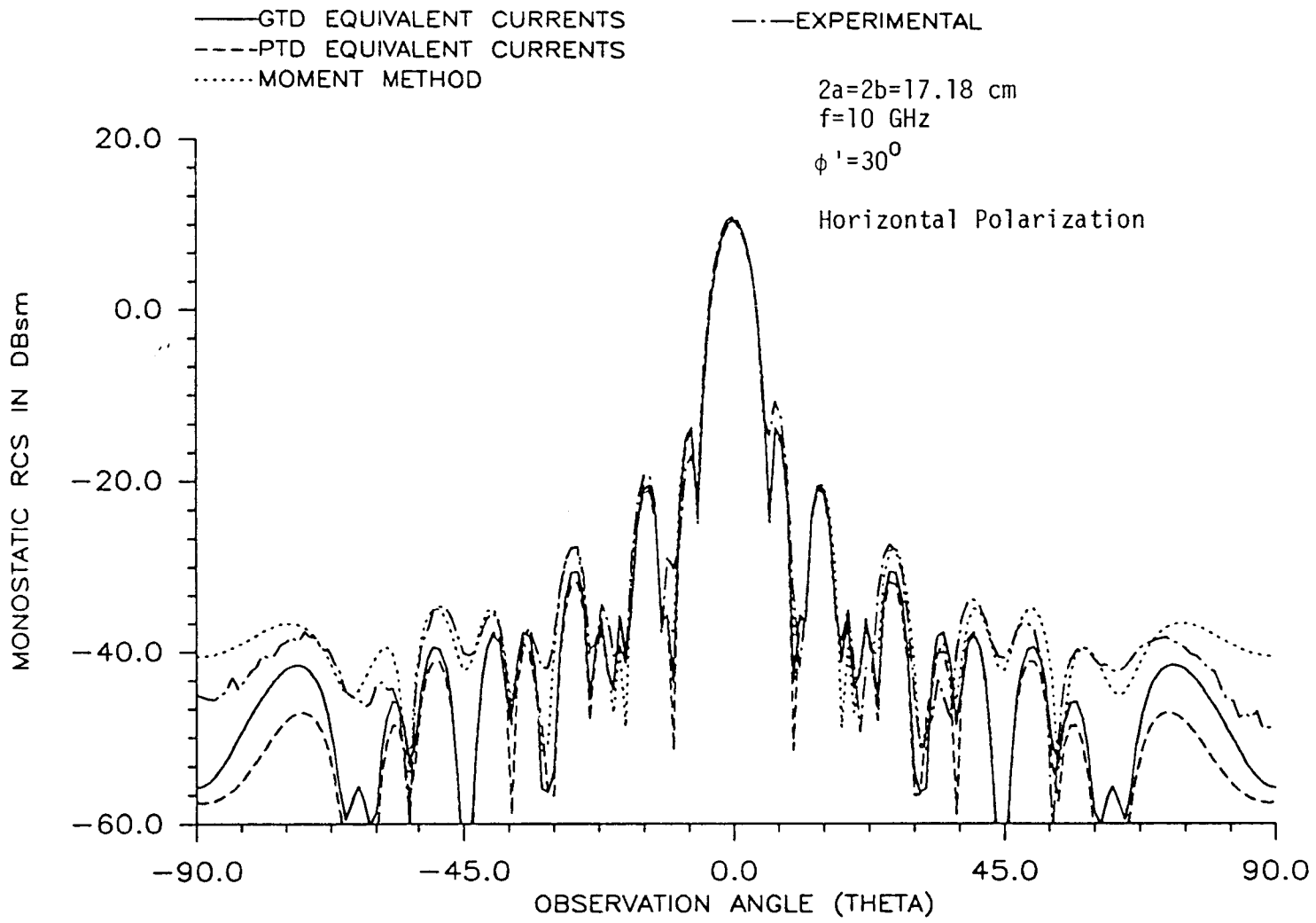

Fig. 4. RCS for a perfectly conducting square plate tilted 30°.

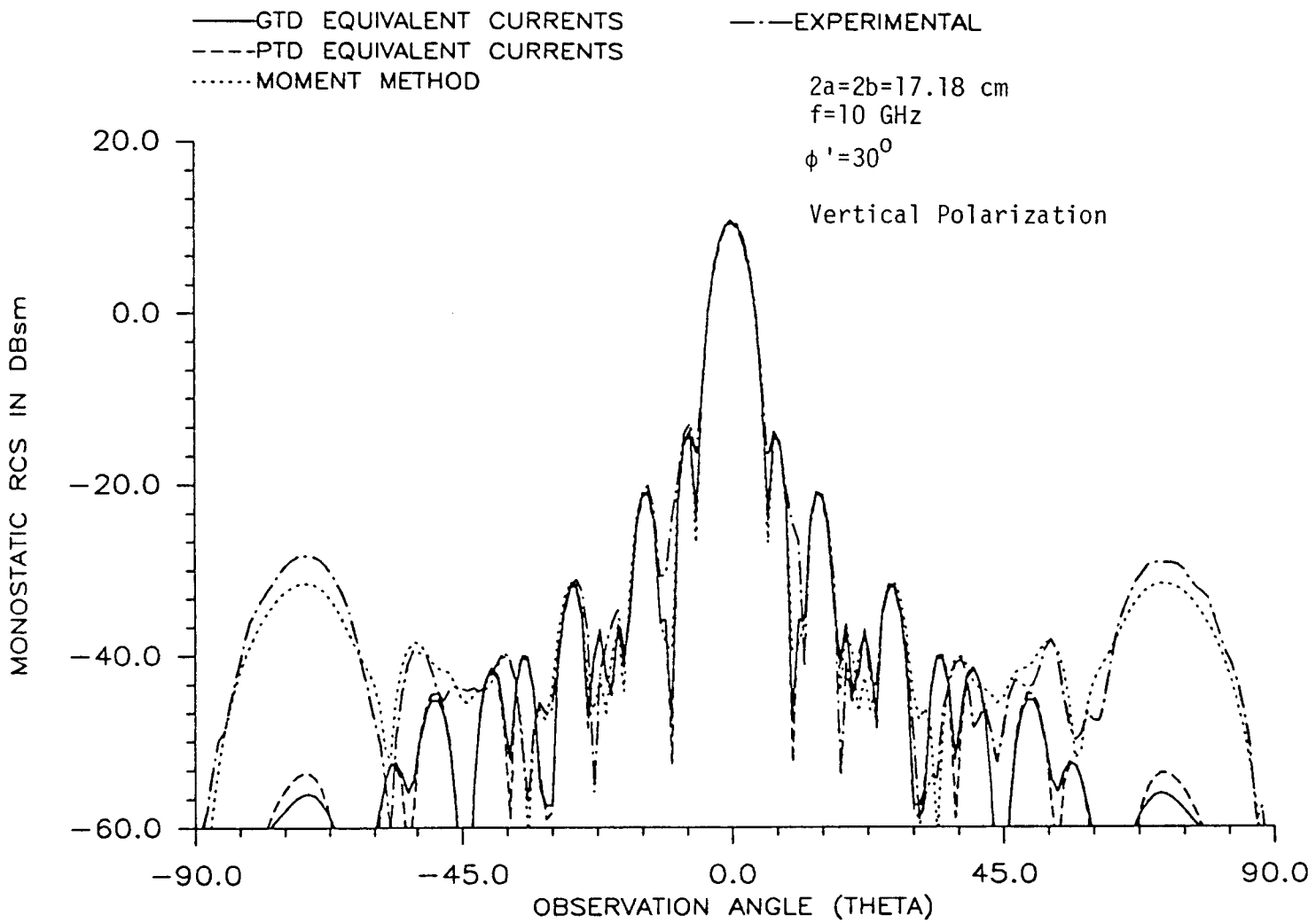

Fig. 5. RCS for a perfectly conducting square plate tilted 30^{o}.

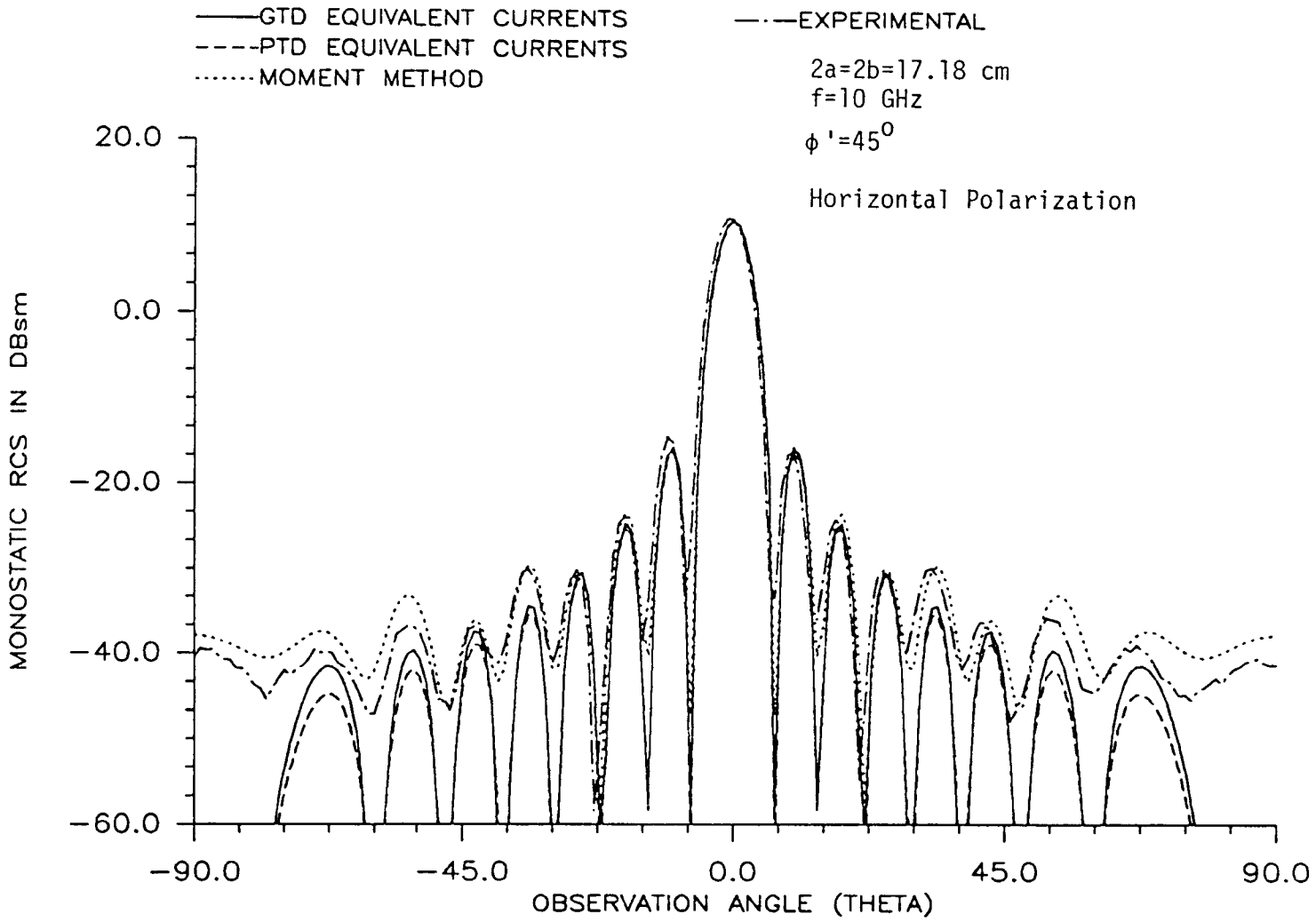

Fig. 6. RCS for a perfectly conducting square plate tilted 45^{o}.

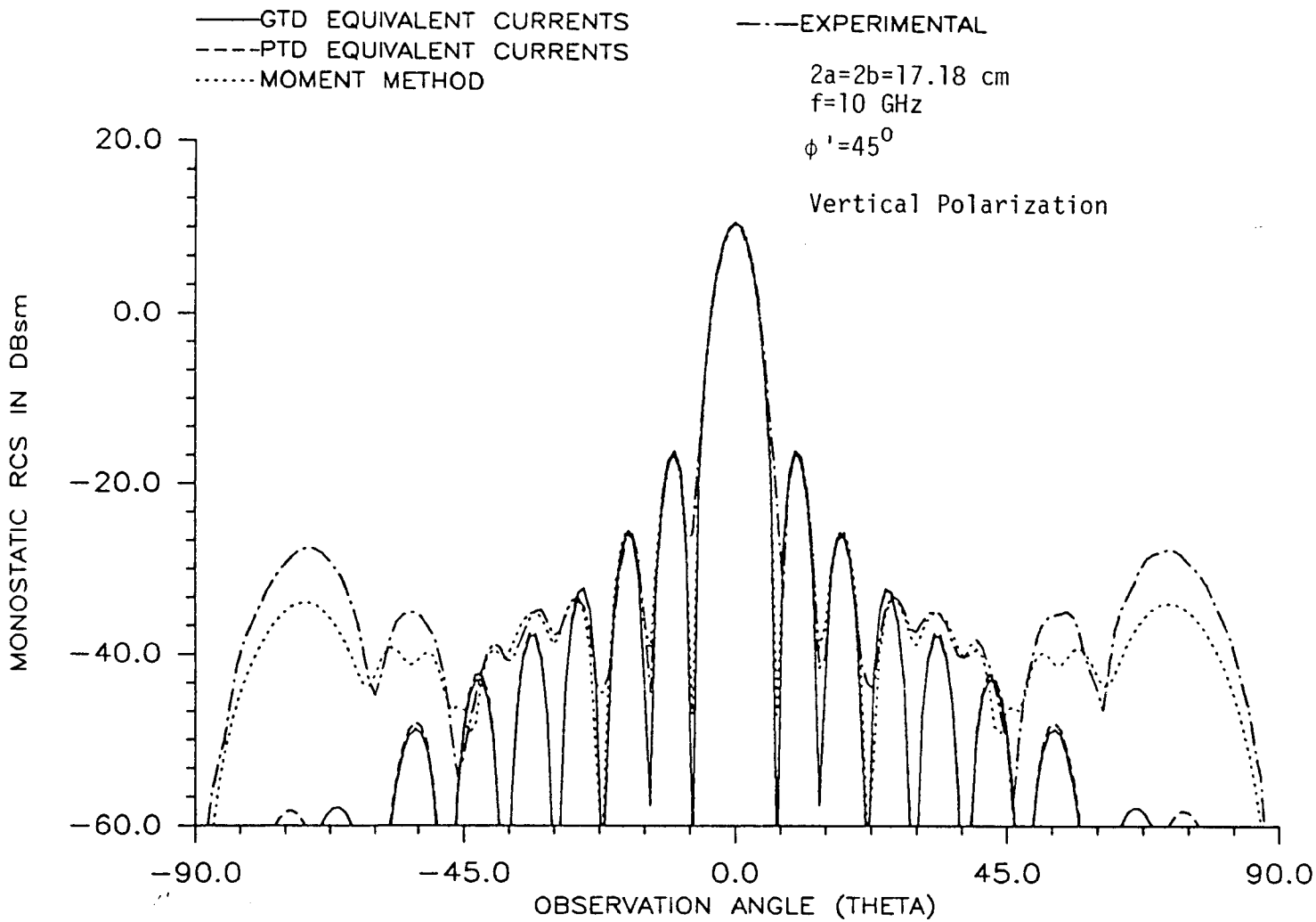

Fig. 7. RCS for a perfectly conducting square plate tilted 45°.

PART B

PATTERN CONTROL OF HORN ANTENNAS

I. INTRODUCTION

Antenna pattern synthesis or the equivalent problem of pattern control has been an attractive research topic in the past three decades[1]-[4]. Particular interest is in the pattern synthesis of antenna arrays[3],[6],[7]. The pattern synthesis of an aperture antenna has not yet been found to have a satisfactory solution.

Early attempts in using the variational approach to optimizing the radiation pattern have been made by Harris et. al. [5]. In [5], the optimization of the radiation pattern at a single direction is resolved, and a conjugated Green's functional distribution for the directivity is suggested. Another attempt in optimizing the aperture antenna amplitude pattern was made by Elliott[6]-[8]. He discretized the continuous aperture distribution, which allowed him to optimize with respect to each element. This resulted in a numerical solution to the problem.

In this report, a functional analysis approach is introduced to the optimization, in a range of directions, of the antenna amplitude radiation pattern. A continuous eigenfunction solution to this problem is found. A demonstration of the use of the eigenfunction is also included.

II. FAR-ZONE ELECTROMAGNETIC FIELDS

A general method of finding the radiation pattern of an antenna can be obtained by considering the contribution of its physical electric current distributions or the equivalent electric and magnetic currents. Without loss of generality, we start with the magnetic field pattern resulting from the distribution of the electric current on a planar structure.

Given the current distribution $\bar{J}(x',y')$, the magnetic field can be expressed as:

$$\bar{H} = \frac{1}{\mu} \nabla \times \bar{A}$$

$$= \frac{1}{\mu} \nabla \times \left[\frac{\mu}{4\pi} \int_S \bar{J}(x',y') \frac{e^{-jkR}}{R} \, dx' dy' \right]$$

$$\bar{H} = \frac{1}{4\pi} \nabla \times \int_S \bar{J}(x',y') \frac{e^{-jkR}}{R} dx' dy' \qquad (1)$$

where $k = \omega(\mu\varepsilon)^{1/2}$ is the wave constant, μ and ε are the permeability and permitivity of the medium, respectively.

Since we only deal with the far-field pattern, we can assume that the observations are made in the far-field of the radiating object. Thus we can write that

$$R = r - x' \sin\theta \cos\phi - y' \sin\theta \sin\phi \qquad (2)$$

where r is the distance between the observation point and the origin of the coordinate. Since we are only concerned with the radiated field component, we can represent the operator ∇ by

$$\nabla \longleftrightarrow -j \bar{k}. \qquad (3)$$

Using (3) reduces (1) to

$$\bar{H} = \frac{e^{-jkr}}{4\pi r}(-j\bar{k}) \times \int_S \bar{J}(x',y')e^{jk\sin\theta(x'\cos\phi + y'\sin\phi)}dx'dy' \qquad (4)$$

We consider a relatively simple case where we observe the field along the plane defined by $\phi = 0$. In addition, we assume that the electric current is directed along the X axis. Thus

$$\bar{k} \times \bar{J} = k\, J(x',y')\cos\theta\, \hat{a}_h \qquad (5)$$

where $\hat{a}_h$ is a unit vector aligned with the total magnetic field. Finally, combining all the constants in (4) into H_o, the magnetic field can be written as

$$\bar{H}[I,\theta] = \hat{a}_h\, H_o\, \cos\theta \int_{x_1}^{x_2} I(x')\, e^{jkx'\sin\theta}\, dx' \qquad (6)$$

where

$$I(x') = \int_{y_1}^{y_2} J(x',y')\, dy' \qquad (6a)$$

$$H_o = \frac{k}{4\pi r} \qquad (6b).$$

The radiated power density pattern is widely used to evaluate the quality of an antenna. In the far zone, the radiated power density is proportional to the square of the magnitude of the radiated magnetic field. Thus we can write that

$$P(\theta) = \alpha \left| \bar{H}[I,\theta] \right|^2 \qquad (7)$$

where α is a proportionality physical constant.

III. VARIATIONAL APPROACH TO PATTERN CONTROL

1. The Construction of the Functional

The optimization of the radiation pattern in a certain range of directions (from θ_1 to θ_2 for example), turns out to be a variational calculus problem having the following functional,

$$J[I(x')] = \int_{\theta_1}^{\theta_2} g(\theta)\ P(\theta)\ d\theta \tag{8}$$

where $g(\theta)$ is a function which can be used to weight the different parts of pattern contributed to the functional. $P(\theta)$ is represented by (7), and it can be expressed as

$$P(\theta) = \alpha\ |\bar{H}[I,\theta]|^2 = \alpha\ \bar{H}[I,\theta] \cdot \bar{H}^*[I,\theta]$$

$$= \alpha \left[H_o\ \cos\theta \int_{x_1}^{x_2} I(s)\ e^{\ jkssin\theta}\ ds \right]$$

$$\cdot \left[H_o^*\ \cos\theta \int_{x_1}^{x_2} I^*(t)\ e^{-jktsin\theta} dt \right]$$

$$P(\theta) = \alpha\ |H_o|^2 \cos^2\theta \int_{x_1}^{x_2}\int_{x_1}^{x_2} I(s)\ I^*(t)\ e^{\ jksin\theta(s-t)} dsdt \tag{9}$$

Substituting (9) into (8) leads to

$$J[I(x')] = \int_{\theta_1}^{\theta_2} g(\theta)\alpha |H_o|^2 \cos^2\theta \left[\int_{x_1}^{x_2}\int_{x_1}^{x_2} I(s) I^*(t) e^{jksin\theta(s-t)} dsdt \right] d\theta \tag{10}.$$

The function inside the middle brackets is a well behaved continuous function with respect to θ. Therefore, we interchange the order of the two integrations; and for simplicity, let

$g(\theta) = 1/(\alpha\ |H_o|^2)$. Choosing $g(\theta)$ to be constant implies that all parts of the radiation pattern are weighted equally. However, $g(\theta)$ may be chosen as a function of θ to weight some directions of the radiation pattern more heavily in the functional (8), which results in a higher optimization level for the given directions. After some obvious simplifications, we have:

$$J[I(x')] = \int_{x_1}^{x_2}\int_{x_1}^{x_2} I(s)I^*(t)\left[\int_{\theta_1}^{\theta_2} \cos^2\theta\ e^{jk\sin\theta(s-t)}\ d\theta\right] ds dt \qquad (11)$$

or

$$J\ [I(x')] = \int_{x_1}^{x_2}\int_{x_1}^{x_2} K(s,t)\ I(s)\ I^*(t)\ ds dt \qquad (12)$$

where

$$K(s,t) = \int_{\theta_1}^{\theta_2} \cos^2\theta\ e^{jk\sin\theta(s-t)}\ d\theta \qquad (12a)$$

Notice that K(s,t) is a self-adjoint kernel which satisfies the following equation:

$$K(s,t) = K^*(t,s) \qquad (13)$$

If the functional in (12) should have an extremal, the variational derivative of (12) must satisfy the following condition:

$$\left.\frac{\delta J[I]}{\delta I}\right|_{s_o} = 0 \qquad \text{for each point } s_o \text{ in the source } I(s) \qquad (14)$$

which is equivalent to

$$\left.\frac{\delta J[I]}{\delta h_1}\right|_{s_o} = 0 \tag{14a}$$

$$\left.\frac{\delta J[I]}{\delta h_2}\right|_{s_o} = 0 \tag{14b}$$

where h_1, h_2 are the real and imaginary variational components of the current distribution $I(x')$, respectively. The variational derivative (12a) can be written as

$$\left.\frac{\delta J[I]}{\delta h_1}\right|_{s_o} = \lim_{\epsilon\to 0} \frac{\int_{x_1}^{x_2}\int_{x_1}^{x_2} K(s,t)\left[\mathbb{I}(s)\,\mathbb{I}^*(t) - I(s)I^*(t)\right]ds\,dt}{\epsilon}$$

$$= \int_{x_1}^{x_2}\left[K(x,s_o)I(x)+K(s_o,x)I^*(x)\right]dx = 0 \tag{15}.$$

where $\mathbb{I}(x) = I(x) + \epsilon\delta(x-s_o)$

Following a similar procedure, (12b) gives

$$\left.\frac{\delta J[I]}{\delta h_2}\right|_{s_o} = \int_{x_1}^{x_2}\left[K(s_o,x)I^*(x)-K(x,s_o)\,I(x)\right]dx = 0 \tag{16}$$

Combining (15) and (16), we have an equation which satisfies the variational condition of

$$\int_{x_1}^{x_2} K(x,s_o)I(x)dx = 0 \tag{17}$$

We can define (17) as the extremal condition.

2. Spectral Analysis of the Extremal Condition

The solvability of the problem for the extremal condition can be analyzed by Fourier transforms. Since $K(x,s_o)$ is a function

of the difference of the two arguments [see (12a)], (17) is actually a convolution integral. Thus, the Fourier transform of (17) turns out to be

$$K(\lambda)\cdot I(\lambda) = 0 \tag{18}$$

where

$$I(\lambda) = \int_{x_1}^{x_2} I(\xi)\, e^{j\lambda\xi}\, d\xi \tag{19}$$

$$K(\lambda) = \int_{x_1}^{x_2} e^{j\lambda\tau}\left[\int_{\theta_1}^{\theta_2} \cos^2\theta\; e^{-jk\tau\sin\theta} d\theta\right] d\tau \tag{20}.$$

To have a non-zero solution to (16), we require that the spectrum of $I(\lambda)$ is perpendicular to the spectrum of $K(\lambda)$. That is to say, $I(\lambda)$ has only a spectral component where $K(\lambda)$ is zero. To find these eigenvalues and their eigenfunctions, we need to find the zeros of equation (20). Interchanging the order of integration, the inside integral can be evaluated. After some simplifications, we have

$$K(\lambda)=\int_{\theta_1}^{\theta_2} \cos^2\theta\, \frac{\sin\left[\frac{(\lambda-k\sin\theta)(x_2-x_1)}{2}\right]}{\lambda - k\sin\theta} e^{-j\left[\frac{(\lambda-k\sin\theta)(x_2+x_1)}{2}\right]} d\theta \tag{19}$$

Without loss of generality, we pick the origin of the coordinate at the center of the aperture. Thus, $x_2 + x_1$ is zero. Also, we denote half of the width as w. Then (20) can be rewritten as

$$K(\lambda) = 2\int_{\theta_1}^{\theta_2} \cos^2\theta\, \frac{\sin[(\lambda-k\sin\theta)w]}{\lambda - k\sin\theta}\, d\theta \tag{22}$$

This can be evaluated numerically. A FORTRAN program was written to do the task. Figure 1 shows the spectrum of $K(\lambda)$ when plotted with $2w = 5\lambda$, $\theta_1 = \pi/16$, and $\theta_2=\pi/2$. Using a numerical root finder to determine the zeros of (22), a set of eigenvalues can be found. Those are denoted as

$$\lambda_1, \lambda_2, \cdots\cdots, \lambda_i, \cdots\cdots\cdots \tag{23}$$

and their corresponding eigenfunctions are

$$e^{-j\lambda_1 x'}, e^{-j\lambda_2 x'}, \cdots, e^{-j\lambda_i x'}, \cdots\cdots \tag{24}$$

The current distribution on the aperture, which satisfies the extremal condition can be expressed as linear combinations of these eigenfunctions.

IV. CONCLUSIONS

1. Solutions

From the work of III, we conclude that the extremals of the control functional can be written as

$$I(x') = \sum_{i=1}^{\infty} C_i \; e^{-j\lambda_i x'} \tag{25}$$

and the corresponding radiation pattern can be expressed as

$$P(\theta) = \alpha \left| \sum_{i=1}^{\infty} C_i \; \cos\theta \; \frac{\sin[(\lambda_i - k\sin\theta)w]}{\lambda_i - k\sin\theta} \right|^2 \tag{26}$$

where λ_i's are the eigenvalues of (22) in III; C_i's are the spectra of each component. We found that (25) and (26) take a surprisingly simple form in their expressions. Although in the case when the source distribution is of the finite extent, the eigenfunctions, obtained by such a procedure, still play an important part. The Ritz method [9] can be used to refine the extremal, and to optimize the C_i's used in (25) and (26).

2. An Example

To demonstrate the derived algorithm, a 5λ aperture antenna was examined. The objective was to optimize the antenna pattern to allow the largest possible percentages of radiated energy into the main beam ($0^\circ \leq \theta \leq 11.25^\circ$ where $\theta = 0^\circ$ is normal to the apperture) while reducing the minor lobe ($11.25^\circ \leq \theta \leq 90^\circ$) energy to the smallest level. Control directivities are chosen to be from $\pi/16$ to $\pi/2$ (since this is only a half space antenna problem).

Figure 1 displays the spectrum of $K(\lambda)$ for this particular design. Notice that the zero, which is the closest to $\lambda=0$, has an eigenvalue of 0.4587. Figure 2 shows three normalized (to their maximum values) radiation patterns of the eigenfunctions which correspond to the first three smallest eigenvalues (in magnitude).

Figure 3 exhibits a comparison of the two pattern-optimization approaches. The solid line is the pattern obtained by using the Green's functional distribution suggested by Harris et. al[5]; it maximized the radiation pattern only at $\theta=0$. The dashed line is the optimization pattern obtained by the method that was outlined here. It reduced the percentages of the radiated energy from $\pi/16$ to $\pi/2$ to a lowest possible limit. Doing this, the beam efficiency of such an antenna is greatly enhanced. Moreover, such a radiation pattern shows a certain flatness along the main radiation beam which most antenna designers would like to have. The electric current distribution chosen for this design is the one which has the smallest eigenvalue (the first eigenpattern in Figure 2).

Figure 4 displays the validity of the method. The solid-line shows the ratio variation, with respect to the eigenvalue, of the energy radiated within the controlled directions to the main-beam while the dashed-line shows the variation of the normalized radiated power with respect to the eigenvalue. The curve shows a minimum ratio at the eigenvalue that we have chosen. Also, from the comparison of the two curves, our algorithm does choose the

best design from the trade-off of the beam efficiency and the maximum radiation power from the main beam.

V. FUTURE WORK

Future work on this project will concentrate on the following:

1. The formulation and the solution of the two-dimensional (or three-dimensional, if needed) functional source distribution for horn antenna pattern control.
2. Studies of resistive tapering and its effect on the aperture field distribution of the horn antenna, and on the overall far-zone radiation pattern.
3. Numerical solution of the exact boundary value problem of the horn antenna. This step is also very important because we need it to demonstrate the resultant optimum pattern.

REFERENCES

1. L. Jun, " A universal method for directivity synthesis," *IEEE Trans. Antennas and Propagat.*, vol. AP-35, pp. 1199-1205, November, 1987.

2. Warren L. Stutzman, "Sidelobe control of antenna patterns," *IEEE Trans. Antennas and Propagat.*,vol. AP-20, pp. 102-104, January, 1972.

3. Roger F. Harrington, "Sodelobe reduction by nonuniform element spacing," *IEEE Trans. Antennas and Propagat.*,vol. AP-2, pp. 187-192, 1961.

4. Robert S. Elliott, *Antennas Theory and Design.* Prentice-Hall, 1981, p. 141.

5. J. H. Harris and H. E. Shanks, "A method for synthesis of optimum directional patterns from nonplanar apertures," *IEEE Trans. Antennas Propagat.*, vol. AP-2, pp. 228-236, May, 1962

6. Robert S. Elliott, "On discretizing continuous aperture distributions," *IEEE Trans. Antennas and Propagat.*,vol. AP-25, pp. 617-621, September, 1977.

7. Robert S. Elliott, "Design of line-source antennas for sum patterns with sidelobe of individual arbitrary heights," *IEEE Trans. Antennas and Propagat.*, vol. AP-24 , pp. 76-83, January,1976.

8. Robert S. Elliott, "Design of line-source antennas for difference patterns with sidelobes of individually arbitrary heights," *IEEE Trans. Antennas and Propagat.*,vol. AP-24, pp. 310-316, May, 1976.

9. I. M. Gelfand and S. V. Fomin, *Calculus of Variations*, Prentice-Hall, 1963, p. 195.

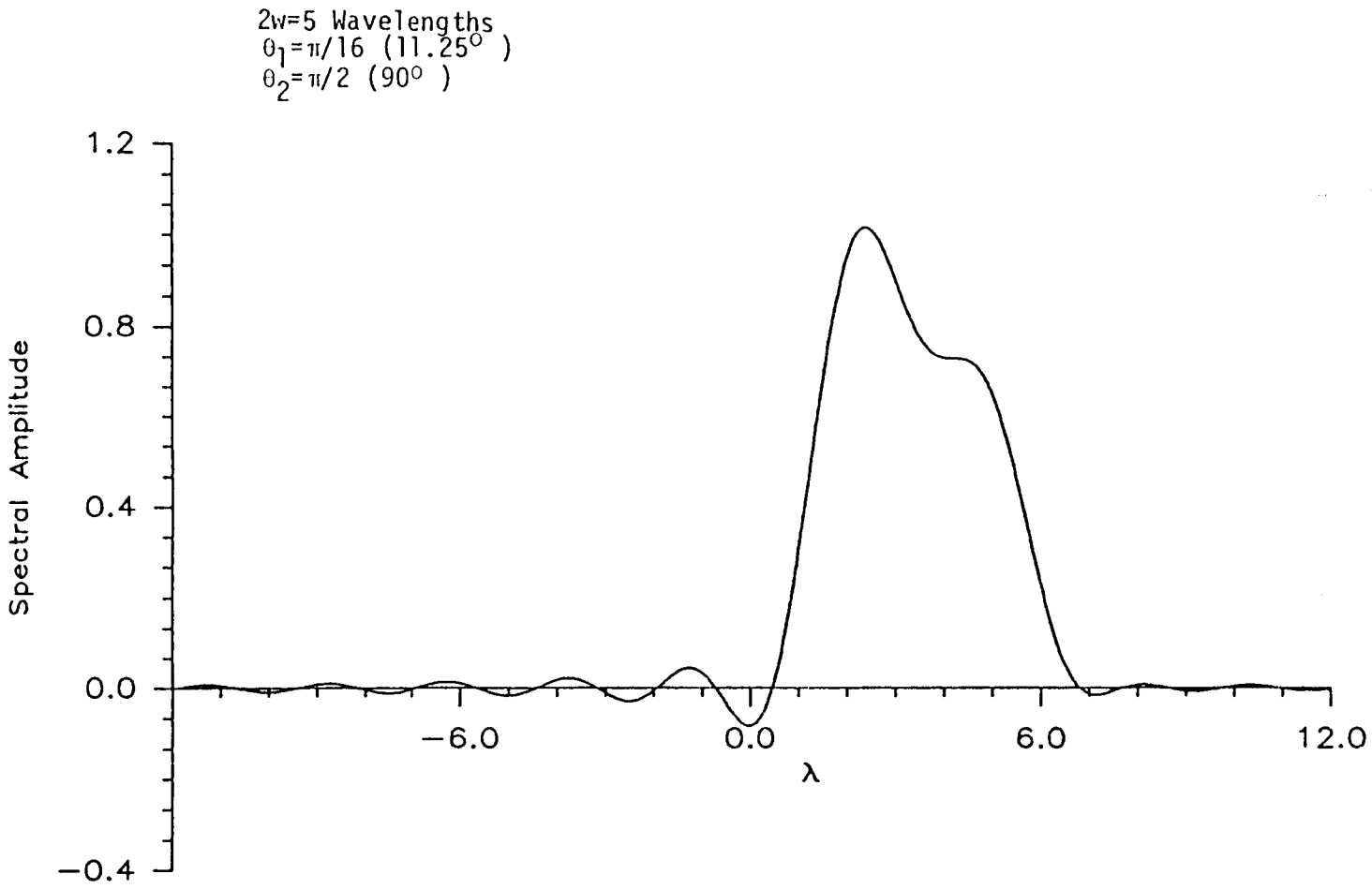

Figure 1. Spectral Distribution of K(λ)

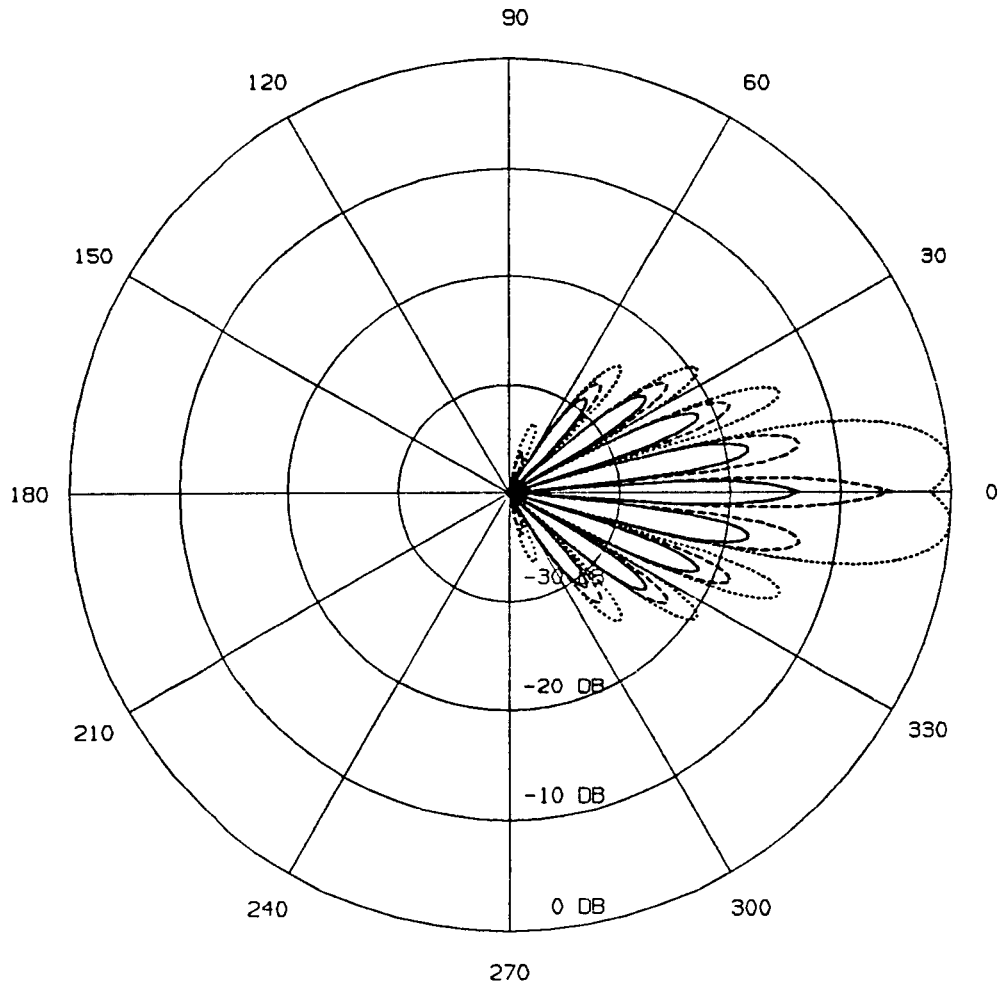

Figure 2. Patterns of the first three eigenfunctions

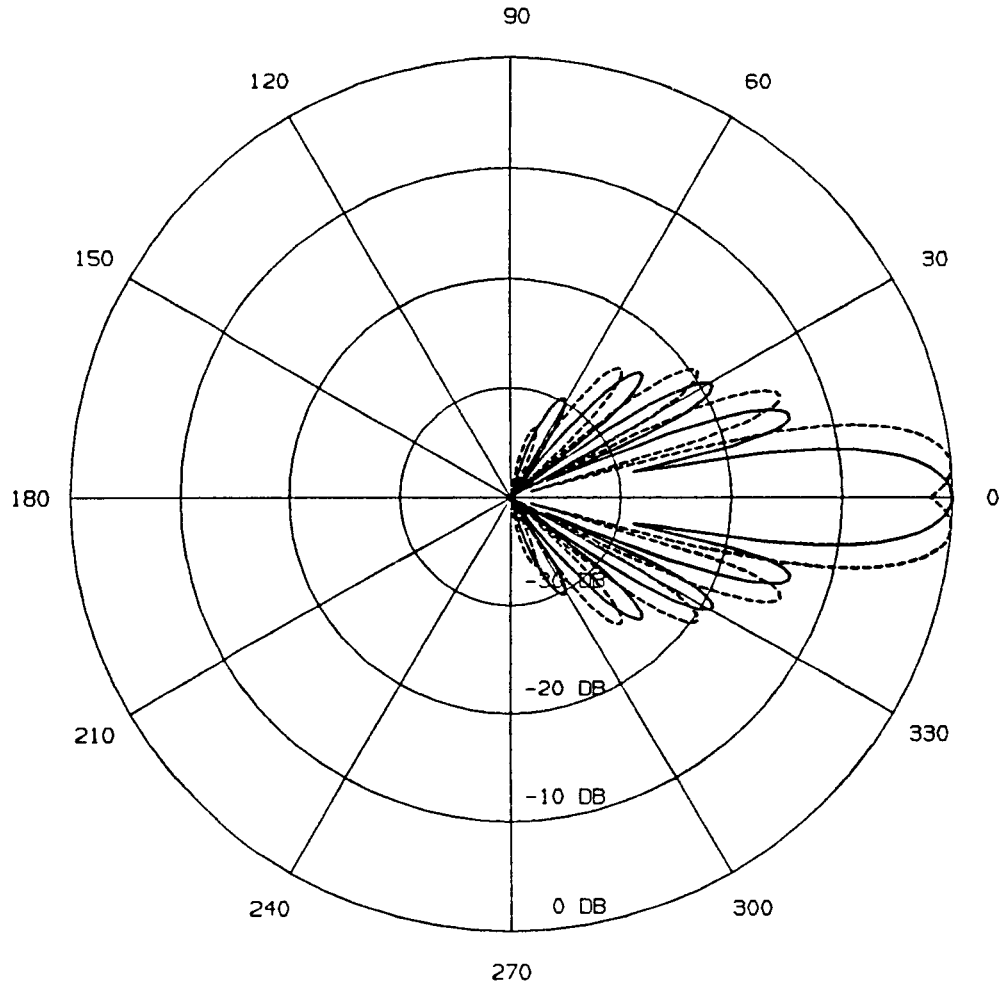

Figure 3. Radiation pattern of Green's functional distribution and the optimum distribution Control between 11.25 to 90 degrees

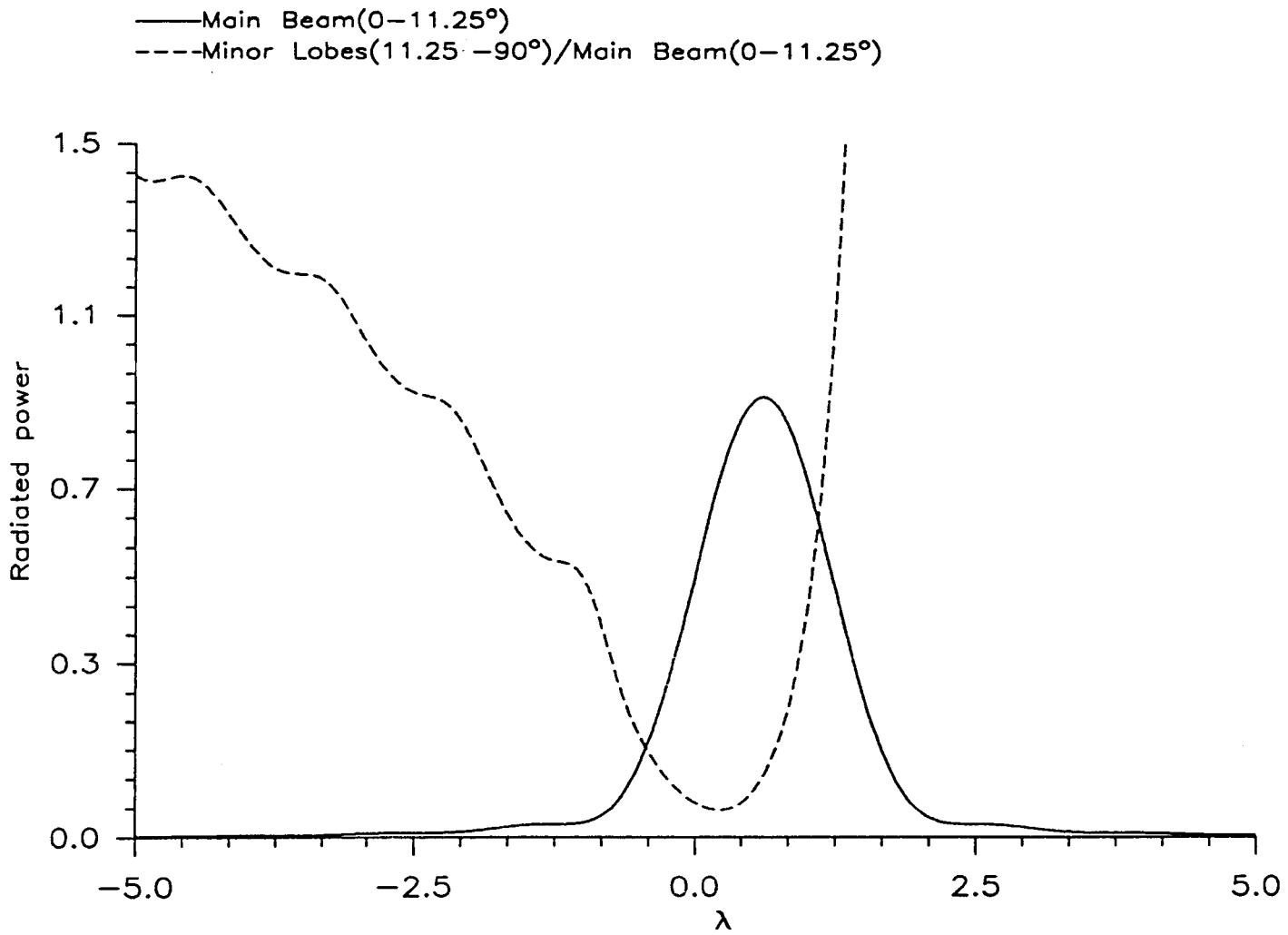

Figure 4. Radiated power of Main beam and minor lobes